Time-Domain Numerical Modeling of Brass Instruments Including Nonlinear Wave Propagation, Viscothermal Losses, and Lips Vibration

H. Berjamin[1)], B. Lombard[1)], C. Vergez[1)], E. Cottanceau[2)]

[1)] Aix-Marseille Univ., CNRS, Centrale Marseille, LMA, Marseille, France.
  lombard@lma.cnrs-mrs.fr

[2)] Arts et Métiers ParisTech, LSIS UMR CNRS 7296, 59046 Lille, France

Summary

A time-domain numerical modeling of brass instruments is proposed. On one hand, outgoing and incoming waves inside the resonator are described by the Menguy-Gilbert model, which incorporates three key features: nonlinear wave propagation, viscothermal losses, and a variable section. The nonlinear propagation is simulated by a finite-volume scheme with flux limiters, well-suited for non-smooth waves. The fractional derivatives induced by the viscothermal losses are replaced by a set of local-in-time memory variables. A splitting strategy is followed to optimally combine these dedicated methods. On the other hand, the exciter is described by a one-mass model for the lips. The Newmark method is used to integrate the nonlinear ordinary differential equation so obtained. At each time step, a coupling is performed between the pressure in the tube and the displacement of the lips. Finally, an extensive set of numerical tests is successfully completed. In particular, self-sustained oscillations of the lips are simulated by taking into account the nonlinear wave propagation in the tube. Simulations clearly indicate that the nonlinear wave propagation has a major influence on the timbre of the sound, as expected. Moreover, simulations also highlight an influence on playing frequencies, time envelopes and on the playability of the low frequencies in the case of a variable lips tension.

PACS no. 43.75.fg, 02.70.Bf

1. Introduction

Risset and Mathews [1] were the first to highlight the fact that the spectral enrichment of brass sounds with increasing sound level is crucial to identifying these instruments. They included nonlinear distortion into their additive sound synthesis more than 10 years before acousticians began to focus on this phenomenon, and 25 years before its origin was understood. In 1980, Beauchamp [2] stressed the fact that a linear model of the air column cannot explain brassy sounds. Since 1996, it has been well established that the spectacular spectral enrichment of loud brass sounds is mainly due to the nonlinear wave propagation inside the bore of the instrument [3, 4, 5]. At extremely high sound levels, shock waves have been observed, but nonlinear distortion even at moderate sound levels can contribute significantly to the timbre of a brass instrument [6, 7].

Considering nonlinear propagation is thus fundamental both to sound synthesis by physical modeling [8, 9, 10, 11]

and to a better understanding of musical instrument design [12, 13, 14]. It is important to take into account the nonlinear wave propagation of both outgoing wave (due to the exciter) and incoming wave (reflected by the bell), unlike some works where the nonlinear propagation only concerns the outgoing wave [15]. To describe the physics of brass instruments, other mechanisms have to be considered, along with nonlinear wave propagation. The issue of the continuous variation of the cross section of the instrument with respect to space has to be dealt with, as well as the even more challenging issue of the viscothermal losses resulting from the interaction between the acoustic field and the bore of the instrument.

Gilbert and coauthors proposed an approach to handle these mechanisms in the periodic regime. The harmonic balance method has been applied to cylinders [16] or tubes of varying cross section [17]. This approach resulted in the development of a simulation tool for brassiness studies [13].

The time domain offers a more realistic framework to simulate instruments in playing conditions, although it raises a number of specific difficulties. Non-smooth (and possibly non-unique) waves are obtained, whose numeri-

cal approximation is not straightforward [18]. Moreover, the viscothermal losses are modeled by fractional derivatives in time [19, 20]. The evaluation of these convolution products requires storing the past values of the solutions, which is highly consuming from a computational point of view.

Time-domain numerical modeling of the coupling between nonlinear propagation, variable section and attenuation has rarely been examined in the literature. Various authors have considered these three features, but in the case of standard non-fractional losses; see [21] and references therein. Nonlinear propagation and fractional losses were examined in the seminal work of Sugimoto [22], but it was in the case of constant cross-section geometry and the approach was essentially theoretical. A numerical extension of this work has been proposed in [23, 24] to investigate the propagation of acoustic solitons in a constant waveguide connected with Helmholtz resonators. The three features were numerically investigated by Bilbao [11, 25]. In particular, he used a discrete filter to simulate the memory effects due to the viscothermal losses in the linear regime. But he examined them separately.

A model of the exciter should also be considered when modelling the instrument and the instrumentalist during steady states and transients. For this purpose, we use a classical one-mass model for the lips [26]. Providing an efficient numerical modeling of this exciter-resonator coupled system, leading to numerical results that can be trusted, is the aim of this article. In addition, the applicative contribution of our work is to demonstrate that the obtained virtual instrument is useful in investigations in musical acoustics.

The paper is organized as follows. Section 2 is devoted to the modeling of the resonator. The acoustic propagation inside the bore of the instrument is described by outgoing and incoming nonlinear simple waves, which interact only at the extremities of the instrument [13]. A so-called diffusive approximation is used to discretize the viscothermal losses efficiently. Then the equations are solved numerically by applying a splitting strategy, which offers a maximal computational efficiency: the propagative part is solved by a finite-volume scheme with flux limiters (a standard scheme in computational fluid dynamics), and the relaxation part is solved exactly. These numerical methods are recalled here, both for the sake of self-contained reading, and because the equations differ partly from the equations investigated in the present work. This section ends with a set of numerical tests; an application to the determination of the input impedance in the linear case is proposed. Section 3 is devoted to the numerical modeling of the exciter. The coupling between the exciter (air blown through vibrating lips) and the resonator (the instrument) is explored in section 4 through various numerical experiments. These experiments will show that this simulation tool offers various possibilities, and will highlight the influence of nonlinear propagation on various aspects of the instrument behavior. Lastly, future lines of research are proposed in section 5.
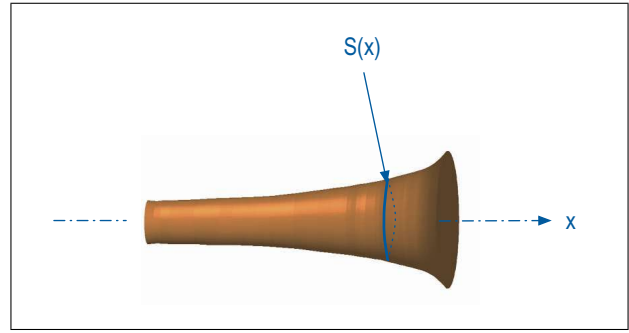

Figure 1. One-dimensional acoustic tube of cross section area $S(x)$.

2. Resonator

2.1. Physical modeling

2.1.1. Notations

A tube with variable radius R depending on the abscissa x is considered. The length of the tube is D and its cross section is S (Figure 1). The physical parameters are the ratio of specific heats at constant pressure and constant volume γ; the pressure at equilibrium p_0; the density at equilibrium ρ_0; the Prandtl number Pr; the kinematic viscosity ν; and the ratio of shear to bulk viscosities μ_v/μ. One deduces the sound speed a_0, the sound diffusivity ν_d and the coefficient of dissipation in the boundary layer C,

$$a_0 = \sqrt{\frac{\gamma\, p_0}{\rho_0}}, \quad \nu_d = \nu\left(\frac{4}{3} + \frac{\mu_v}{\mu} + \frac{\gamma - 1}{\text{Pr}}\right),$$
$$C = 1 + \frac{\gamma - 1}{\sqrt{\text{Pr}}}. \tag{1}$$

2.1.2. Menguy-Gilbert model

The angular frequency of the disturbance is below the first cut-off angular frequency ($\omega < \omega^* = \frac{1.84\, a_0}{R_{\max}}$ where $R_{\max}$ is the maximum radius), so that only the plane mode propagates and the one-dimensional assumption is satisfied [27]. The framework of weakly nonlinear acoustics is followed. Moroever, the radius is assumed to vary sufficiently slowly on the scale of variation of a wavelength: $\frac{\lambda}{2\pi}\left|\frac{R'}{R}\right| \ll 1$, with $\lambda = 2\pi a_0/\omega$. Then the wave field is split into simple outgoing waves (denoted $+$) and incoming waves (denoted $-$) that do not interact during their propagation [28, 17].

Velocities along the x-axis are denoted $u^\pm$. Pressure fluctuations associated with the simple waves are given by

$$p^\pm = \pm\rho_0\, a_0\, u^\pm. \tag{2}$$

According to the Menguy-Gilbert model, the evolution equations satisfied by the velocities are

$$\begin{cases} \dfrac{\partial u^\pm}{\partial t} + \dfrac{\partial}{\partial x}\left(\pm a u^\pm + b\dfrac{(u^\pm)^2}{2}\right) \pm \dfrac{a}{S}\dfrac{\mathrm{d}S}{\mathrm{d}x}u^\pm \\[2mm] \quad = \pm c\,\dfrac{\partial^{-1/2}}{\partial t^{-1/2}}\dfrac{\partial u^\pm}{\partial x} + d\dfrac{\partial^2 u^\pm}{\partial x^2}, \quad 0 < x < D, \quad (3\text{a}) \\[2mm] u^+(0, t) = u_0(t), \hspace{3.7cm} (3\text{b}) \\[2mm] u^-(D, t) = u^+(D, t), \hspace{3cm} (3\text{c}) \end{cases}$$

with the coefficients

$$a = a_0, \quad b = \frac{\gamma + 1}{2}, \quad c(x) = \frac{C\, a_0 \sqrt{\nu}}{R(x)}, \quad d = \frac{\nu_d}{2}. \quad (4)$$

Menguy-Gilbert's equation (3a) takes into account nonlinear advection (coefficients a and b), viscothermal losses at walls (coefficient c) and volume dissipation (coefficient d) [29, 16]. The operator $\frac{\partial^{-1/2}}{\partial t^{-1/2}}$ is the Riemann-Liouville fractional integral of order $1/2$. For a causal function $w(t)$, it is defined by

$$\begin{aligned} \frac{\partial^{-1/2}}{\partial t^{-1/2}} w(t) &= \frac{H(t)}{\sqrt{\pi\, t}} * w, \\ &= \frac{1}{\sqrt{\pi}} \int_0^t (t - \tau)^{-1/2}\, w(\tau)\, \mathrm{d}\tau, \end{aligned} \quad (5)$$

where $*$ denotes the convolution product, and $H(t)$ is the Heaviside function [20].

Each wave requires only one boundary condition. The condition for the outgoing wave (3b) models the acoustic source, linked to the musician. The condition for the incoming wave (3c) models the Dirichlet condition on pressure at the bell. This condition is the unique coupling between + and − wave.

2.1.3. Dispersion analysis

Applying space and time Fourier transforms to (3a) yields

$$\begin{aligned} &i\, d\, k^2 \widehat{u^\pm} \pm \left((a - c\chi(\omega))\, \widehat{u^\pm} \pm \frac{b}{2} \widehat{(u^\pm)^2} \right) k \\ &-\omega\, \widehat{u^\pm} \pm i\, \frac{a}{S} \frac{\widehat{\mathrm{d}S}}{\mathrm{d}x} u^\pm = 0, \end{aligned} \quad (6)$$

where the hat refers to the transforms, k is the wavenumber, and χ is the symbol of the $1/2$-integral,

$$\chi(\omega) = \frac{1}{(i\,\omega)^{1/2}}. \quad (7)$$

In the case of constant radius R, linear propagation ($b = 0$), and no sound diffusivity ($d = 0$), the phase velocity $v = \omega / \mathrm{Re}(k)$ and the attenuation $\alpha = -\mathrm{Im}(k)$ of an outgoing wave are deduced explicitly,

$$\begin{aligned} v &= \frac{a^2\, \omega - a\, c\sqrt{2\,\omega} + c^2}{a\,\omega - c\sqrt{\omega/2}}, \\ \alpha &= \frac{c}{\sqrt{2}} \frac{\omega^{3/2}}{a^2\,\omega - a\,c\,\sqrt{2\,\omega} + c^2}. \end{aligned} \quad (8)$$

In the case where the viscosity is ignored ($c = d = 0$), the phase velocity is equal to a, and no attenuation occurs. Otherwise, one obtains

$$\begin{aligned} v(\omega) &\underset{0}{\sim} -c\sqrt{\frac{2}{\omega}}, & \lim_{\omega \to +\infty} v(\omega) &= a, \\ \alpha(0) &= 0, & \alpha(\omega) &\underset{+\infty}{\sim} \frac{c}{a^2}\sqrt{\frac{\omega}{2}}. \end{aligned} \quad (9)$$

2.2. Mathematical modeling

2.2.1. Diffusive approximation

The half-order integral (5) in (3a) is non-local in time. It requires to keeping the memory of the past history of the solution, which is very costly in numerical computations. As in [23, 24], an alternative approach is followed here, based on the diffusive representation of the fractional integral. A change of variables yields [19, 30]

$$\frac{\partial^{-1/2}}{\partial t^{-1/2}} w(t) = \int_0^{+\infty} \phi(t, \theta)\, \mathrm{d}\theta, \quad (10)$$

where the memory variable ϕ such that

$$\phi(t, \theta) = \frac{2}{\pi} \int_0^t e^{-(t-\tau)\, \theta^2}\, w(\tau)\, \mathrm{d}\tau \quad (11)$$

satisfies the ordinary differential equation

$$\begin{cases} \dfrac{\partial \phi}{\partial t} = -\theta^2\, \phi + \dfrac{2}{\pi}\, w, \\ \phi(0, \theta) = 0. \end{cases} \quad (12)$$

The diffusive representation (10) replaces the non-local term (5) by an integral on θ of functions $\phi(t, \theta)$, which are solutions of local-in-time equations. Integral (10) is then approximated by a quadrature formula

$$\frac{\partial^{-1/2}}{\partial t^{-1/2}} w(t) \simeq \sum_{\ell=1}^{L} \mu_\ell\, \phi(t, \theta_\ell) = \sum_{\ell=1}^{L} \mu_\ell\, \phi_\ell(t), \quad (13)$$

on L quadrature points. Determining the quadrature weights μ_ℓ and the nodes θ_ℓ is crucial for the efficiency of the diffusive approximation and will be discussed further in section 2.3.1.

2.2.2. First-order system

Following [23, 24], the $1/2$-integral in (3a) is replaced by its diffusive approximation (13) and by the set of differential equations satisfied by the memory functions ϕ_ℓ (12). As a result, the two systems for + and − waves write

$$\begin{cases} \dfrac{\partial u^\pm}{\partial t} + \dfrac{\partial}{\partial x}\left(\pm a u^\pm + b\, \dfrac{(u^\pm)^2}{2} \right) \pm \dfrac{a}{S}\dfrac{\mathrm{d}S}{\mathrm{d}x}\, u^\pm \\ \qquad = \pm c \displaystyle\sum_{\ell=1}^{L} \mu_\ell \phi_\ell + d\, \dfrac{\partial^2 u^\pm}{\partial x^2}, \quad 0 < x < D, \quad (14a) \\[2mm] \dfrac{\partial \phi_\ell^\pm}{\partial t} - \dfrac{2}{\pi} \dfrac{\partial u^\pm}{\partial x} = -\theta_\ell^2\, \phi_\ell^\pm, \quad \ell = 1, \ldots, L, \quad (14b) \\[2mm] u^+(0, t) = u_0(t), \quad (14c) \\[2mm] u^-(D, t) = u^+(D, t), \quad (14d) \\[2mm] u(x, 0) = v(x), \quad \phi_\ell(x, 0) = 0, \quad \ell = 1, \ldots, L. \quad (14e) \end{cases}$$

The $(L + 1)$ unknowns are gathered in the vectors $\mathbf{U}^\pm$:

$$\mathbf{U}^\pm = \left(u^\pm, \phi_1^\pm, \cdots, \phi_L^\pm \right)^T. \quad (15)$$

Then the systems (14) are recast as:

$$\frac{\partial}{\partial t}\mathbf{U}^{\pm} + \frac{\partial}{\partial x}\mathbf{F}^{\pm}(\mathbf{U}^{\pm}) = \mathbf{S}^{\pm}\,\mathbf{U}^{\pm} + \mathbf{G}\,\frac{\partial^2}{\partial x^2}\mathbf{U}^{\pm}, \qquad (16)$$

where $\mathbf{F}^{\pm}$ are the nonlinear flux functions

$$\mathbf{F}^{\pm}(\mathbf{U}^{\pm}) = \left(\pm a u^{\pm} + b\frac{(u^{\pm})^2}{2}, -\frac{2}{\pi}u^{\pm}, \cdots, -\frac{2}{\pi}u^{\pm}\right)^{T} \quad (17)$$

and $\mathbf{G}$ is the $(L+1)\times(L+1)$ diagonal matrix with terms $\mathrm{diag}(d, 0, \cdots, 0)$. The relaxation matrices $\mathbf{S}^{\pm}$ include both a geometrical term, due to the variation of section, and physical terms, related to the diffusive approximation of viscothermal losses:

$$\mathbf{S}^{\pm} = \begin{pmatrix} \mp\frac{a}{S}\frac{\mathrm{d}S}{\mathrm{d}x} & \pm c\,\mu_1 & \cdots & \pm c\,\mu_L \\ 0 & -\theta_1^2 & & \\ \vdots & & \ddots & \\ 0 & & & -\theta_L^2 \end{pmatrix}. \qquad (18)$$

2.2.3. Properties

In brass musical instruments, the volume losses are negligible compared to the viscothermal losses [22, 16]. Consequently, the qualitative behavior of the solutions to (16) is essentially unchanged when taking $\mathbf{G} = \mathbf{0}$ (we neglect the volume attenuation only in this section, for theoretical purposes). In this case, the properties of the solutions rely on the Jacobian matrices $\mathbf{J}^{\pm} = \frac{\partial \mathbf{F}^{\pm}}{\partial \mathbf{U}^{\pm}}$. Some properties are listed here without proof; interested readers are referred to standard textbooks for more details about hyperbolic systems [31, 18].

The eigenvalues $\lambda_j^{\pm}$ of $\mathbf{J}^{\pm}$ are real $(j = 1, \ldots, L+1)$,

$$\lambda_1^{\pm} = \pm a + b\,u^{\pm}, \quad \lambda_j^{\pm} = 0; \qquad (19)$$

Assuming $\lambda_1^{\pm} \neq 0$, the matrices of eigenvectors $\mathbf{R}^{\pm} = (\mathbf{r}_1^{\pm}|\mathbf{r}_2^{\pm}|\ldots|\mathbf{r}_{L+1}^{\pm})$ are

$$\mathbf{R}^{\pm} = \begin{pmatrix} 1 & 0 \cdots 0 \\ \frac{-2}{\pi\,(\mp a + bu^{\pm})} & 1 \\ \vdots & & \ddots \\ \frac{-2}{\pi\,(\mp a + bu^{\pm})} & & & 1 \end{pmatrix}, \qquad (20)$$

and they are invertible provided $u^{\pm} \neq \pm a/b$, which is consistent with the assumption of weak nonlinearity: the systems (16) are hyperbolic, but not strictly hyperbolic (multiple eigenvalues). The characteristic fields satisfy $(j = 1, \ldots, L+1)$:

$$\nabla \lambda_1 . \mathbf{r}_1^{\pm} = b \neq 0, \quad \nabla \lambda_j . \mathbf{r}_j^{\pm} = 0, \qquad (21)$$

where the gradient is calculated with respect to each coordinate of $\mathbf{U}$ in (15), as defined in [32, p77]. Consequently, there exists one genuinely nonlinear characteristic field, and L linearly degenerate characteristic fields.

Moreover, the eigenvalues of the relaxation matrices $\mathbf{S}^{\pm}$ are $(j = 1, \ldots, L+1)$:

$$\kappa_1 = \mp\frac{a}{S}\frac{\mathrm{d}S}{\mathrm{d}x}, \quad \kappa_j = -\theta_j^2. \qquad (22)$$

Assuming that the quadrature nodes are sorted by increasing order $(\theta_1 < \theta_2 < \cdots < \theta_L)$, the spectral radius of $\mathbf{S}^{\pm}$ is

$$\varrho(\mathbf{S}^{\pm}) = \max\left(\max_{x\in[0,D]}\frac{a}{S}\frac{\mathrm{d}S}{\mathrm{d}x}, \theta_L^2\right). \qquad (23)$$

Lastly, a Fourier analysis of (14) leads to a dispersion relation similar to (6). The symbol χ in (7) needs only to be replaced by the symbol of the diffusive approximation

$$\tilde{\chi}(\omega) = \frac{2}{\pi}\sum_{\varrho=1}^{L}\frac{\mu_\varrho}{\theta_\varrho^2 + i\,\omega}. \qquad (24)$$

2.3. Numerical modeling

2.3.1. Quadrature methods

Various strategies exist to determine the quadrature weights μ_ϱ and nodes θ_ϱ in (13), which are involved in the relaxation matrices (18). Here we follow the same approach as in [24], where a nonlinear optimisation with constraint of positivity on the symbols (7) and (24) is used. The cost function

$$\begin{aligned} \mathcal{J}\left(\{(\mu_\varrho, \theta_\varrho)\}_\varrho; L, K\right) &= \sum_{k=1}^{K}\left|\frac{\tilde{\chi}(\omega_k)}{\chi(\omega_k)} - 1\right|^2 \\ &= \sum_{k=1}^{K}\left|\frac{2}{\pi}\sum_{\varrho=1}^{L}\mu_\varrho\frac{(i\omega_k)^{1/2}}{\theta_\varrho^2 + i\omega_k} - 1\right|^2, \end{aligned} \qquad (25)$$

is minimized with respect to the parameters $\{(\mu_\varrho, \theta_\varrho)\}_\varrho$ for $\varrho = 1, \ldots, L$, on a given angular frequency range $[\omega_{\min}, \omega_{\max}]$. Doing so makes it possible to achieve high accuracy with a minimum number L of diffusive variables. The reader is refered to [24] for technical details.

2.3.2. Numerical scheme

As in [23, 24], we follow a splitting strategy to integrate (16); doing so provides an optimal condition of stability, independently of the variations in cross-section and of the fractional attenuation. Equations (16) are split into a propagative step

$$\frac{\partial}{\partial t}\mathbf{U}^{\pm} + \frac{\partial}{\partial x}\mathbf{F}(\mathbf{U}^{\pm}) = \mathbf{G}\,\frac{\partial^2}{\partial x^2}\mathbf{U}^{\pm}, \qquad (26)$$

and a relaxation step

$$\frac{\partial}{\partial t}\mathbf{U}^{\pm} = \mathbf{S}^{\pm}\,\mathbf{U}^{\pm}. \qquad (27)$$

The discrete operators associated with (26) and (27) are denoted by $\mathbf{H}_a^{\pm}$ and $\mathbf{H}_b^{\pm}$ respectively. Strang splitting is

then used to make a step forward from t_n to t_{n+1} by solving successively (26) and (27) with adequate time steps [31],

$$
\begin{aligned}
\mathbf{U}_j^{(1)\pm} &= \mathbf{H}_b^{\pm}\left(\tfrac{\Delta t}{2}\right)\mathbf{U}_j^{(n)\pm},\\
\mathbf{U}_j^{(2)\pm} &= \mathbf{H}_a^{\pm}\left(\Delta t\right)\mathbf{U}_j^{(1)\pm},\\
\mathbf{U}_j^{(n+1)\pm} &= \mathbf{H}_b^{\pm}\left(\tfrac{\Delta t}{2}\right)\mathbf{U}_j^{(2)\pm}.
\end{aligned}
\tag{28}
$$

Equation (26) corresponding to the propagative part is solved using a finite-volume scheme with flux limiters [18],

$$
\begin{aligned}
\mathbf{U}_i^{(n+1)\pm} = \mathbf{U}_i^{(n)\pm} &- \frac{\Delta t}{\Delta x}\left(\mathbf{F}_{i+1/2}^{\pm} - \mathbf{F}_{i-1/2}^{\pm}\right)\\
&+ \mathbf{G}\frac{\Delta t}{\Delta x}\left(\mathbf{U}_{i+1}^{(n)\pm} - 2\mathbf{U}_i^{(n)\pm} + \mathbf{U}_{i-1}^{(n)\pm}\right),
\end{aligned}
\tag{29}
$$

where $\mathbf{F}_{i\pm1/2}^{\pm}$ is the numerical flux function for Burger's equation in (17). This scheme is a nonlinear combination between the second-order Lax-Wendroff scheme and the first-order Godunov scheme. Practically, it results in an order slightly smaller than 2.

At time t_n, one defines the maximum numerical velocity $a_{\max}^n$ and the discrete Péclet number Pe

$$
a_{\max}^n = \max |\pm a + bu_j^{(n)\pm}|, \quad \mathrm{Pe} = a_{\max}^n \frac{\Delta x}{2\,d} \gg 1. \tag{30}
$$

Then, the discrete operator $\mathbf{H}_a^{\pm}$ in (29) is stable under the Courant-Friedrichs-Lewy (CFL) condition [33]

$$
\varepsilon = \frac{a_{\max}^n \Delta t}{\Delta x}\left(1 + \frac{1}{\mathrm{Pe}}\right) \le 1. \tag{31}
$$

Thanks to the splitting strategy, the value of Δt is not penalized by the spectral radius of $\mathbf{S}^{\pm}$. It must be noted that (31) follows from a linearised analysis, and thus it is only a necessary condition of stability. To our knowledge, rigorous proofs are obtained only in the particular case of scalar homogeneous hyperbolic equations [34]. In the case tackled here, many numerical tests of stability have confirmed that (31) is a necessary and sufficient condition.

Equation (27) of the diffusive part is solved exactly,

$$
\mathbf{H}_b^{\pm}\left(\tfrac{\Delta t}{2}\right)\mathbf{U}_j^{\pm} = \exp\left(\mathbf{S}^{\pm}\tfrac{\Delta t}{2}\right)\mathbf{U}_j^{\pm}, \tag{32}
$$

with the matrix exponential deduced from (18)

$$
e^{\mathbf{S}^{\pm}\tau} = \tag{33}
$$

$$
\begin{pmatrix}
e^{-\Omega^{\pm}\tau} & \delta_1^{\pm}\left(e^{-\Omega^{\pm}\tau} - e^{-\theta_1^2\tau}\right) & \cdots & \delta_L^{\pm}\left(e^{-\Omega^{\pm}\tau} - e^{-\theta_L^2\tau}\right) \\
0 & e^{-\theta_1^2\tau} & & \\
\vdots & & \ddots & \\
0 & & & e^{-\theta_L^2\tau}
\end{pmatrix},
$$

and the coefficients ($\ell = 1, \ldots, L$)

$$
\Omega^{\pm} = \pm\frac{a}{S}\frac{\mathrm{d}S}{\mathrm{d}x}, \quad \delta_\ell^{\pm} = \pm\frac{c\,\mu_\ell}{\theta_\ell^2 - \Omega^{\pm}}. \tag{34}
$$

Table I. Physical parameters of air at $15\,°\mathrm{C}$.

γ	p_0 (Pa)	ρ_0 (kg/m^3)	Pr	v (m^2/s)	μ_v/μ
1.403	10^5	1.177	0.708	$1.57\cdot10^{-5}$	0.60

This relaxation step is unconditionally stable. Without viscothermal losses ($c = 0$), the matrix exponential (34) degenerates towards the scalar $e^{-\Omega^{\pm}\tau}$. The physically-realistic case $\mathrm{d}S/\mathrm{d}x > 0$ yields a decreasing amplitude of u^+ as x increases. Inversely, it yields an increasing amplitude of u^- as x decreases.

The Jacobian matrices and the relaxation matrices do not commute: $\mathbf{J}^{\pm}\mathbf{S}^{\pm} \neq \mathbf{S}^{\pm}\mathbf{J}^{\pm}$. In this case, an additional second-order error of splitting is introduced before any discretization [31]. Since the schemes used to solve (26) and (27) are respectively of order 2 and of order infinite, second-order accuracy is obtained at best when solving the splitting. It is stable under the CFL condition (31).

2.4. Numerical tests

2.4.1. Configuration

In all the tests, one considers a circular tube of length $D = 1.4$ m, with an entry radius $R(0) = 7$ mm. The physical parameters given in Table I are used to determine the coefficients (4) in (14a). The tube is discretized on $N_x = 400$ points in space. At each time step, the numerical solution is recorded at four receivers uniformly distributed along the tube, located at $x_r = 0.4\,(i - 1)$ m, with $i = 1, \ldots, 4$.

At each iteration, the time step Δt is deduced from the condition (31), where the CFL number is $\varepsilon = 0.95$. Taking $\varepsilon = 0.95$ instead of 1 ensures that no instabilities are excited by round-off errors.

The exciting source in (14c) is a smooth combination of truncated sinusoidal wavelets,

$$
u_0(t) = \begin{cases} V\displaystyle\sum_{m=1}^4 a_m \sin\left(b_m\,\omega_c\,t\right) & \text{if } 0 \le t \le \frac{1}{f_c},\\ 0 & \text{else}, \end{cases} \tag{35}
$$

with amplitude $V = 20$ m/s, central frequency $f_c = \omega_c/2\pi = 1$ kHz and coefficients $b_m = 2^{m-1}$, $a_1 = 1$, $a_2 = -21/32$, $a_3 = 63/768$ and $a_4 = -1/512$.

2.4.2. Diffusive approximation

The first test investigates the accuracy of the diffusive approximation to model fractional viscothermal losses (section 2.3.1). The nonlinearity and the volume attenuation are neglected ($b = 0$, $d = 0$), and the radius R is constant. Based on the discussion of section 2.3.1, a comparison is performed between a modified Gauss-Jacobi quadrature and an optimized quadrature. The reference solution is the phase velocity of the linear Menguy-Gilbert model (8), where the symbol χ is given by (7). Conversely, the phase velocity of the diffusive model relies on the symbol (24).

Figure 2a compares these different phase velocities, using $L = 6$ memory variables. Large errors are obtained
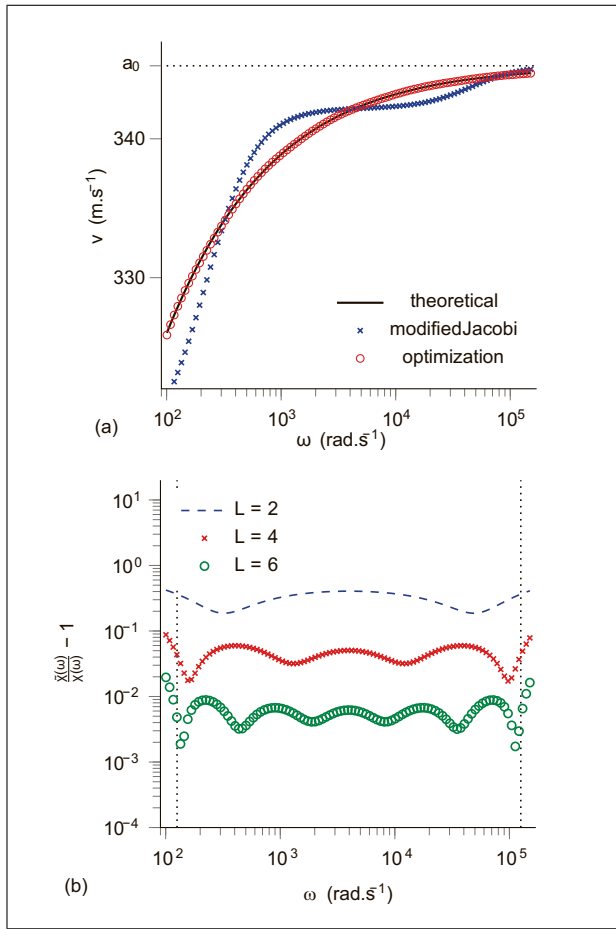
(a)

(b)

Figure 2. Approximation of the fractional derivative. (i) Phase velocity of the Menguy-Gilbert model (3) and of the diffusive model (14). The horizontal dotted line denotes the sound velocity a_0. (ii) Error $|\tilde{\chi}(\omega)/\chi(\omega) - 1|$. Vertical dotted lines show the limits of the range $[\omega_{min}, \omega_{max}]$ where the diffusive approximation is optimized.

when the modified Gauss-Jacobi quadrature is used. On the contrary, the agreement between exact and approximate phase velocities is far better when the optimisation with constraint is used. In this latter case, the optimization range $[\omega_{min}, \omega_{max}]$ is set to [125.66, 125663.70] rad/s, which corresponds to the audio range [20 Hz, 20 kHz]. This interval is used in forthcoming experiments.

From now on, optimization with constraint is chosen. To see the error induced by the optimization more clearly (25), Figure 2b displays the modeling error $|\tilde{\chi}(\omega)/\chi(\omega) - 1|$ on a logarithmic scale. The optimization of the coefficients (μ_ℓ, θ_ℓ) is performed with different numbers of memory variables L. The error decreases by a factor of approximately 10 when L is doubled. In the following numerical experiments, the viscothermal losses have been accounted for by $L = 6$ memory variables.

2.4.3. Simulation of an input impedance

The coupling between the advection and the diffusive approximation of the viscothermal losses is studied here. A constant radius $R = 7$ mm is considered. Linear wave propagation is assumed ($b = 0$). When the outgoing wave
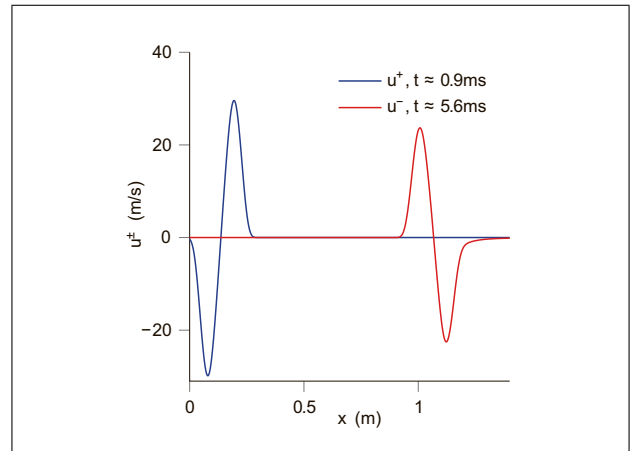

Figure 3. Snapshot of the outgoing and incoming velocities at to different times, where propagation is linear and the tube has a constant cross section area.

reaches the limit of the tube ($x = D$), the incoming wave is generated and propagates along the decreasing x. The velocity is displayed at two different times on Figure 3. Due to the viscothermal losses, the amplitude of the wave diminishes during the simulation and the waveform is no longer symmetrical, which illustrates the dispersive nature of the propagation.

The outgoing pressure $p^+(0, t_n)$ emitted by the exciting source is known. A receiver at $x = 0$ records the pressure $p^-(0, t_n)$ up to $t = 0.1$ s. Zero-padding of $p^\pm$ is done up to 1.34 s, leading to 131072 samples and to a frequency step $\Delta f = 0.744$ Hz. Fourier transforms in time of $p^\pm$ yield an estimate of the input impedance Z of the tube,

$$Z(\omega) = Z_c \frac{1 + r(\omega)}{1 - r(\omega)}, \qquad (36)$$

with

$$Z_c = \frac{\rho_0 a_0}{S}, \qquad r(\omega) = \frac{\widehat{p^-}(0, \omega)}{\widehat{p^+}(0, \omega)}. \qquad (37)$$

Figure 4 shows the modulus and the phase of the input impedance deduced from the numerical simulations. These quantities are compared to their analytical approximation given by [27]

$$Z = i Z_c \tan(kD), \qquad k = \frac{\omega}{a_0} - i(1 + i) 3 \cdot 10^{-5} \frac{\sqrt{f}}{R}. \qquad (38)$$

The location and the magnitude of the upper peaks of impedance's modulus are given in Table II, up to 1 kHz. The maximal error of location is smaller than 0.8 Hz (peak 11). Errors of magnitude decrease monotonically, from 2.02% at peak 1 to 0.08% at peak 15.

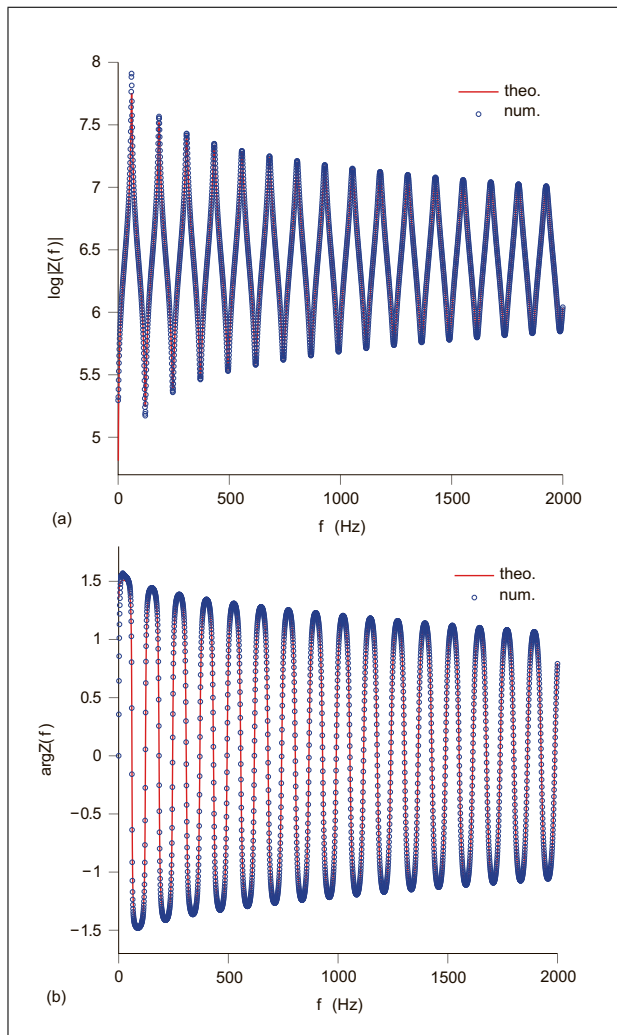The third test focuses on a variable cross section area $S(x)$, with a

Figure 4. Input impedance Z: modulus (i) and phase (ii). Comparison between simulated and exact values.

Table II. Modulus of the input impedance: comparison between exact and numerical values at the peaks n. Frequency F, amplitude A and relative error ϵ. The tilde denotes the numerical value.

n	F (Hz)	$\tilde{F}$ (Hz)	ϵ_F (%)	A	$\tilde{A}$	ϵ_A (%)
1	60.28	60.28	0.00	7.90	7.75	2.02
3	183.84	183.84	0.00	7.56	7.51	0.63
5	308.13	308.13	0.00	7.43	7.40	0.34
7	431.69	432.43	0.17	7.35	7.33	0.25
9	555.99	556.73	0.13	7.29	7.28	0.20
11	680.28	681.03	0.11	7.24	7.23	0.15
13	805.33	805.33	0.00	7.21	7.20	0.11
15	929.62	929.62	0.00	7.17	7.17	0.08

2.4.4. Linear propagation with a varying cross section area

radius varying exponentially from $R(0) = 7$ mm to $R(D) = 2\,R(0)$,

$$S(x) = \pi \left(R(0)\, 2^{x/D} \right)^2, \quad 0 \le x \le D. \qquad (39)$$

It yields $\lambda/(2\pi)|R'/R| = 0.0273 \ll 1$, which validates the use of a 1D model [35]. Linear propagation is assumed
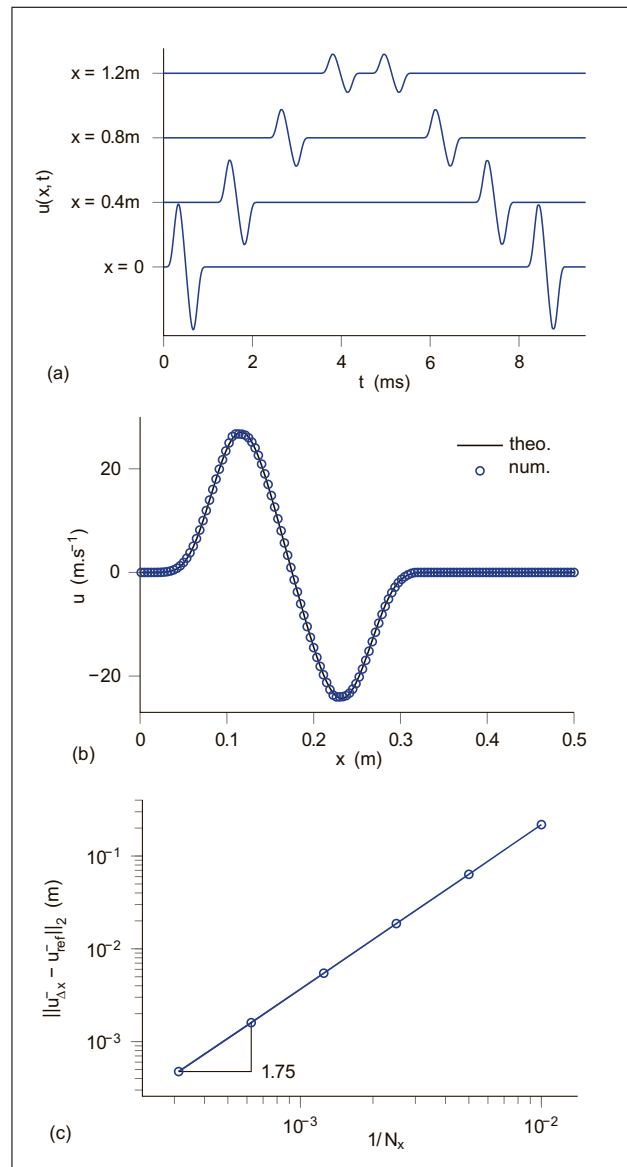

Figure 5. Tube with exponentially-varying cross section area (39). Linear wave propagation in a tube with variable cross section. (i): seismogram of $u = u^+ + u^-$ at the four receivers. (ii): comparison between numerical and exact values of u^- at $t = 7$ ms. (iii): convergence measurements.

($b = 0$), and the dissipation effects are neglected ($c = 0$, $d = 0$). The discretization of the variable radius involves the relaxation parts of the splitting (28): only the component $e^{-\Omega^\pm \tau}$ in (34) is non-null. The exact solution is deduced from the method of characteristics,

$$u^+(x, t) = \exp\left(-\Omega^+ \frac{x}{a}\right) u_0 \left(t - \frac{x}{a}\right). \qquad (40)$$

The seismogram in Figure 5a shows the time history of the total velocity $u = u^+ + u^-$ at the four receivers. At each receiver, the first wavefront corresponds to u^+, and then it is followed by u^-. Since the section of the tube increases with x, (40) implies that the amplitude of u^+ decreases when considering the successive receivers. On the contrary, the incoming wave u^- experiences a decreasing
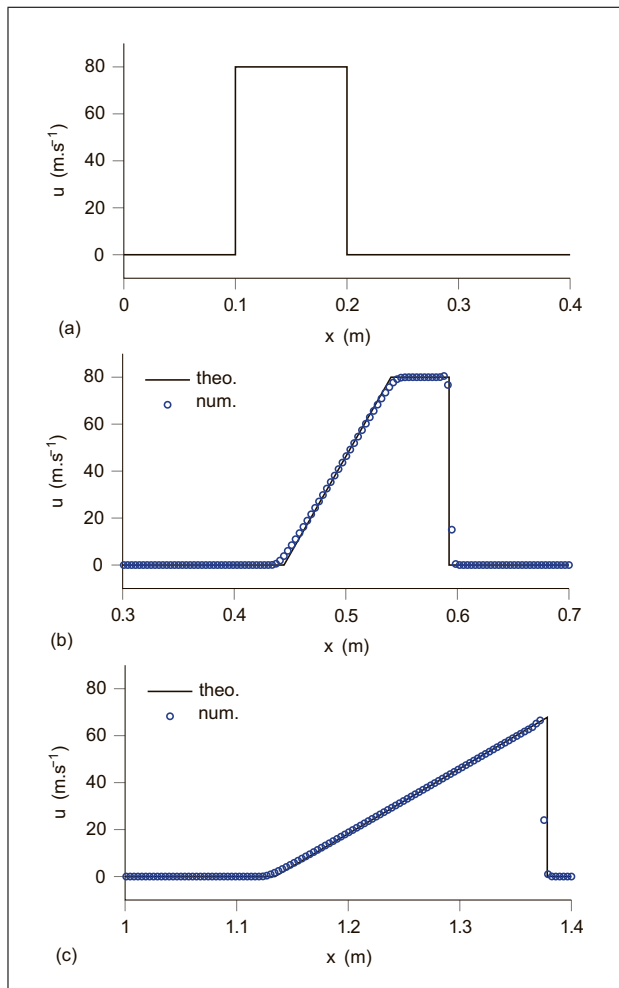
Figure 6. Nonlinear wave propagation. (i) Initial data $v(x)$. (ii) comparison between exact and numerical values of the outgoing velocity at $t \approx 1$ ms. (iii) idem at $t \approx 3$ ms.

section as it propagates leftwards. It results that the amplitude of u^- increases from $x_r = 1.2$ m to $x_r = 0$ m. On each receiver, one observes that the amplitudes of u^+ and u^- are the same, at the scale of the figure. This confirms that the numerical dissipation introduced by the numerical scheme is very small for this discretization.

Figure 5b compares the numerical and exact values of u^- at $t = 7$ ms. Lastly, measures of errors are obtained for various discretizations, from $N_x = 100$ to $N_x = 3200$. The evolution of the L_2 norm in terms of N_x is shown on Figure 5c in log-log scale. As predicted theoretically, the measured order of convergence is 1.75.

2.4.5. Nonlinear propagation

Now we test the modeling of nonlinear waves with the finite-volume scheme (29). For this purpose, losses are neglected ($c = 0$, $d = 0$), and the radius of the tube is constant. The forcing in (14c) is null. The initial data (14e) is a rectangular pulse with a 80 m/s amplitude and a wavelength $\lambda = 0.1$ m.

Figure 6 displays the numerical solution and the exact solution at various instants. The exact solution is derived from the elementary solutions to the Riemann problem
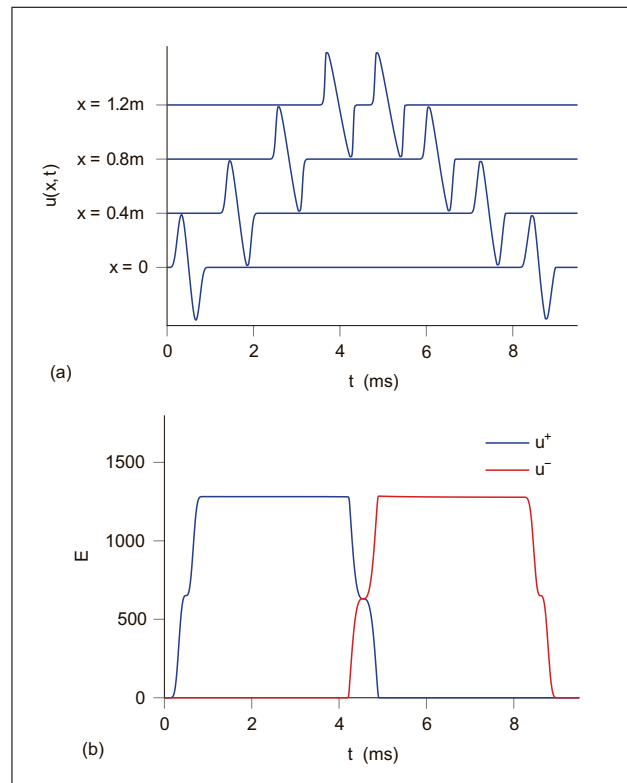

Figure 7. Nonlinear propagation in a constant cylinder, without attenuation. Amplitude of forcing $V = 6$ m/s (35). Top: seismogram of $u = u^+ + u^-$. Bottom : time history of the energy.

[36]. In (ii), one observes an outgoing shock wave followed by a rarefaction wave. In (iii), the rarefaction has reached the shock. In each case, agreement is observed between numerics and analytics, despite the non-smoothness of the solution. In particular, the shock propagates at the right speed, which reveals that the Rankine-Hugoniot condition is correctly taken into account.

A similar test has already been investigated in Figure 8d of [23], but on a much finer grid. It is important to observe the effect of the discretization on the shock wave and rarefaction wave. In particular, one observes that the shock is smeared over about two grid nodes, which characterizes the quality of the numerical scheme at the typical frequencies studied here.

2.4.6. Complete Menguy-Gilbert model

In a last set of experiments, the nonlinear propagation of the outgoing and incoming waves is investigated. First, a cylinder with constant radius is considered, and we neglect attenuation as in section 2.4.5. Two amplitudes of the source (35) are chosen, in order to illustrate the generation of shocks. Taking $V = 6$ m/s (Figure 7), one observes the sharpening of u^+; but the shock formation does not happen until the wave reaches the end of the tube, so the oncoming wave recovers the original shape and amplitude of the outgoing wave. Let us define the discrete energy at time t_n,

$$E^n = \sum_{j=0}^{N_x} \left(\left(u_j^{(n)+} \right)^2 + \left(u_j^{(n)-} \right)^2 \right). \tag{41}$$
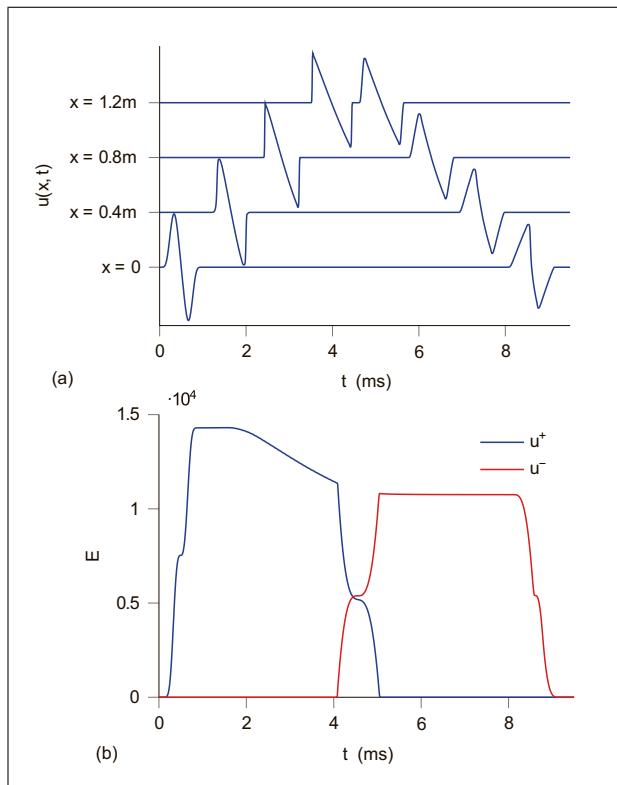
Figure 8. Nonlinear propagation in a constant cylinder, without attenuation. Amplitude of forcing $V = 20$ m/s (35). Top: seismogram of $u = u^+ + u^-$. Bottom: time history of the energy.
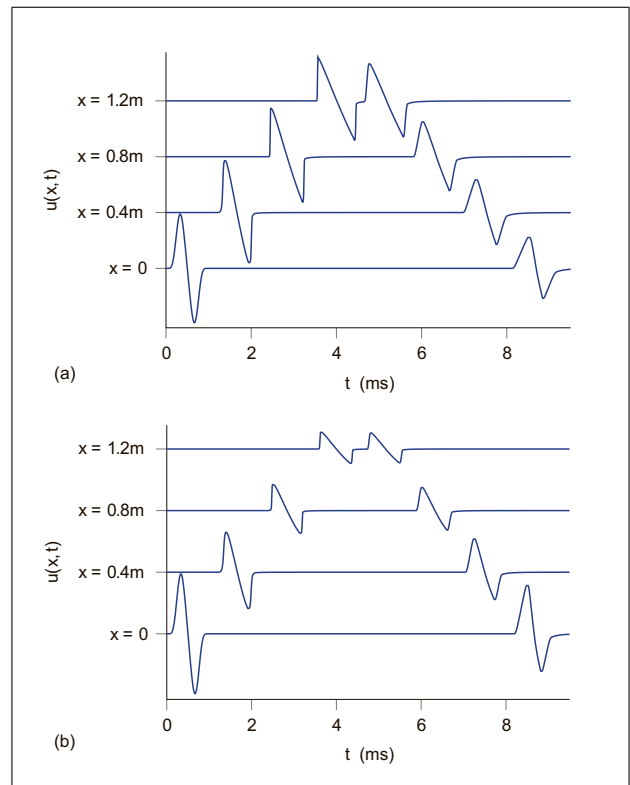

Figure 9. Nonlinear propagation with attenuation and amplitude of forcing $V = 20$ m/s (35): seismogram of $u = u^+ + u^-$. Top: constant cylinder. Bottom: variable section.

At the scale of the figure, the energy of the outgoing wave is entirely transmitted to the incoming wave. On the contrary, $V = 20$ m/s (Figure 8) leads to an irreversible shock. Near $t = 1.8$ ms, one observes a decrease of energy due to the formation of the shock in u^+. The incoming wave u^- unfolds, but cannot recover the original shape and amplitude of the source, due to the loss of energy.

Attenuation is taken into account in Figure 9, where the forcing amplitude is $V = 20$ m/s. The top figure illustrates the case of a constant radius. Logically, the amplitude of waves is slightly reduced compared with the inviscid case shown on Figure 8. Moreover, the viscothermal losses are insufficient to prevent the occurrence of shocks, as predicted in [22].

Lastly, the bottom of Figure 9 illustrates the case where all the effects are taken into account: nonlinear wave propagation with large amplitude $V = 20$ m/s, variable cross section, and attenuation. As in Figure 5a, the amplitude of the incoming wave increases as it propagates leftwards. This effect counterbalances the decrease in amplitude due to the attenuation and to the occurrence of a shock.

3. Exciter

3.1. Physical modeling

The musician's lips are modeled by a one-mass mechanical oscillator at the entry of the resonator [26]. Only the vertical displacement of the upper lip is modeled; the interaction with the static lower lip is ignored. The upper lip is modeled by a thin rigid rectangular plate of height h and width l. It makes an angle φ with the horizontal x-axis, so that the projected surface of the lip on the vertical axis is

$$A = h\, l \sin\varphi. \tag{42}$$

A spring with stiffness k and a damper with coefficient r are put over the lip of mass m (Figure 10). The pressure in the musician's mouth is $p_m(t)$; the acoustical pressure p_e at the entry of the resonator ($x = 0$) depends upon the opening y of the lips and upon the time t,

$$\begin{aligned} p_e(y, t) &= p_e^+(y, t) + p_e^-(y, t), \\ &= p^+(0, t) + p^-(0, t), \end{aligned} \tag{43}$$

The balance of forces yields the ordinary differential equation satisfied by y,

$$\begin{cases} m\ddot{y} + r\dot{y} + k(y - y_{eq}) = f(y, t), & \text{(44a)} \\ y(0) = y_0, \quad \dot{y}(0) = y_1, & \text{(44b)} \end{cases}$$

where y_{eq} is the equilibrium position of the free oscillator,

$$f(y, t) = A\, (p_m(t) - p_e(y, t)) \tag{45}$$

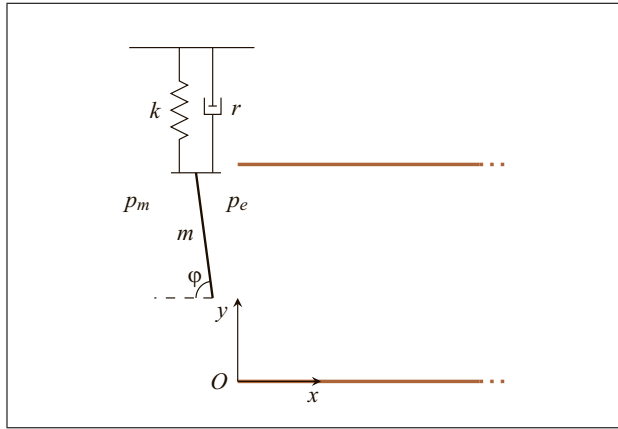is the aeroacoustic force applied to the lip, and (y_0, y_1) are the initial conditions.

Figure 10. One-mass model for the lips.

The flow is assumed to be stationary, incompressible, laminar and inviscid in the musician's mouth and under the lip. Consequently, Bernoulli's equation and the conservation of mass can be applied. The sudden cross section variation behind the lip creates a turbulent jet which dissipates all its kinetic energy in the mouthpiece without pressure recovery [37]. It follows [38, 39]

$$
p_e(y,t) = \begin{cases} 2p_e^- - \dfrac{\xi}{2}\psi y \left(\psi y - \sqrt{\psi^2 y^2 + 4\left| p_m - 2p_e^- \right|} \right) \\ \qquad\qquad\qquad\qquad \text{if } y > 0, \\ 2p_e^- \qquad\qquad\qquad\quad\ \text{if } y \le 0. \end{cases} \tag{46}
$$

The coefficients in (47) are

$$
\begin{aligned}
\xi(y,t) &= \operatorname{sgn}\big(p_m(t) - p_e(y,t)\big) \\
&= \operatorname{sgn}\big(p_m(t) - 2p_e^-(y,t)\big)
\end{aligned} \tag{47}
$$

and

$$
\psi = l\, Z_c \sqrt{\frac{2}{\rho_0}} = l\sqrt{2\rho_0}\,\frac{a_0}{S(0)}. \tag{48}
$$

Existence and uniqueness of the solution for (45)–(47) is proven in the appendix H-4 of [39].

3.2. Numerical modeling

3.2.1. Numerical scheme

The numerical integration of (44) relies on a variable time step Δt_n, noted Δt for the sake of simplicity; as shown further in section 4.1, it is the time step used for wave propagation in the resonator. The approximation of the exact solution $y(t_n)$ is denoted y_n. Similarly, $\dot{y}(t_n)$ and $\ddot{y}(t_n)$ are approximated by $\dot{y}_n$ and $\ddot{y}_n$, respectively.

The Newmark method is applied to (44). This method has recently been used in the context of musical instruments modeling [40]. It relies upon two coefficients β and η, and is second-order accurate in the case of linear forcing. The values $\beta = 1/4$ and $\eta = 1/2$ lead to an unconditionally stable method [41], equivalent to the trapezoidal method. The scheme so-obtained is also second-order accurate, and it conserves the energy.

The predicted values of y_{n+1} and $\dot{y}_{n+1}$ are computed from the known values at time t_n,

$$
\begin{aligned}
\tilde{y}_{n+1} &= y_n + \Delta t\, \dot{y}_n + (1 - 2\beta)\frac{\Delta t^2}{2}\, \ddot{y}_n, \\
\tilde{\dot{y}}_{n+1} &= \dot{y}_n + (1 - \eta)\,\Delta t\, \ddot{y}_n.
\end{aligned} \tag{49}
$$

The corrected values at time t_{n+1} are

$$
\begin{aligned}
y_{n+1} &= \tilde{y}_{n+1} + \beta\,\Delta t^2\, \ddot{y}_{n+1}, \\
\dot{y}_{n+1} &= \tilde{\dot{y}}_{n+1} + \eta\,\Delta t\, \ddot{y}_{n+1}.
\end{aligned} \tag{50}
$$

To compute (50), one needs $\ddot{y}_{n+1}$. For this purpose, the corrected values (50) are injected into (44a), yielding the displacement of the lip at time t_{n+1},

$$
\begin{aligned}
y_{n+1} &= \tilde{y}_{n+1} \\
&+ \beta\,\Delta t^2\, \frac{f(y_{n+1}, t_{n+1}) - r\,\tilde{\dot{y}}_{n+1} - k\,(\tilde{y}_{n+1} - y_{eq})}{m + r\,\eta\,\Delta t + k\,\beta\,\Delta t^2}.
\end{aligned} \tag{51}
$$

The aeroacoustic force $f(y,t)$ in (45)–(47) depends nonlinearly upon y. Consequently, the displacement y_{n+1} in (51) is the solution of the fixed point equation

$$
g(z) = z, \tag{52}
$$

with

$$
\begin{aligned}
g(z) &= \tilde{y}_{n+1} \\
&+ \beta\,\Delta t^2\, \frac{f(z, t_{n+1}) - r\,\tilde{\dot{y}}_{n+1} - k\,(\tilde{y}_{n+1} - y_{eq})}{m + r\,\eta\,\Delta t + k\,\beta\,\Delta t^2}.
\end{aligned} \tag{53}
$$

A fixed-point method is used to solve (52). It is initialized by y_n, and then it is performed as long as the relative variation in (52) does not exceed 10^{-13}. At each step of the fixed-point method, one takes $p_e^-(z, t_{n+1}) = p_0^{(n+1)-}$ in (53): this value of the incoming pressure at node 0 and time t_{n+1} is known, based on the propagation step in the resonator (section 2.3.2). The coefficient ξ follows from (47).

Once the displacement y_{n+1} is known, the acceleration is updated based on (50),

$$
\ddot{y}_{n+1} = \frac{y_{n+1} - \tilde{y}_{n+1}}{\beta\,\Delta t^2}. \tag{54}
$$

The velocity $\dot{y}_{n+1}$ is deduced from (50) and (54).

3.2.2. Numerical tests

No closed-form solution of (44) is known. To assess the accuracy of the Newmark method, we consider the linear case of a step forcing: $f(y,t) = H(t)$. The parameters are those in table III, where the initial conditions are $y_0 = y_{eq} = 0$ m and $y_1 = 0$ m/s. The numerical solution is computed on $N_t = 64$ time steps, up to 10 ms (here $\Delta t = 10/64$ ms is constant). Figure 11a compares the
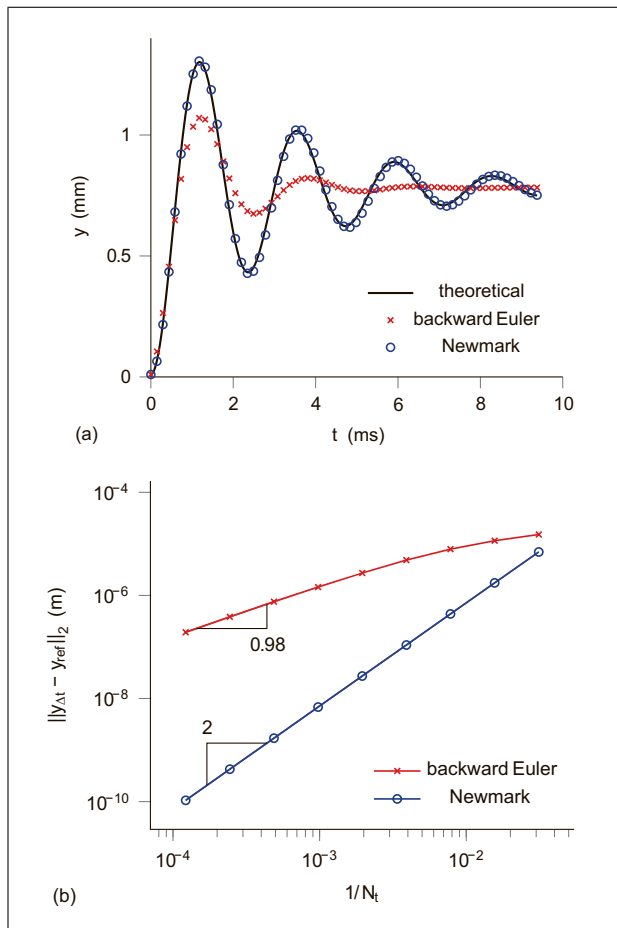
(a)

(b)

Figure 11. Numerical resolution of the ordinary differential equation (44) with a linear step forcing. (i): time histories of the numerical and exact solutions; (ii): convergence measurements.

Newmark solution with the exact solution. For completeness, the solution obtained by the backward Euler first-order method is also displayed. Agreement is obtained between the Newmark solution and the exact solution; on the contrary, the Euler solution suffers from massive numerical dissipation, as expected.

Convergence measurements are performed by considering various numbers of time steps, from $N_t = 32$ to $N_t = 8192$, and by computing the numerical solution up to 10 ms. The errors between the numerical solutions and the exact solution are displayed on Figure 11b in log-log scales. Second-order accuracy is obtained with Newmark's method, whereas only first-order acuracy is obtained with Euler's method.

4. Numerical experiments

4.1. Summary of the algorithm

Here we sum up the coupling between the resonator and the exciter. Time-marching from time t_n to t_{n+1} is as follows ($i = 0, \cdots, N_x$):
1. Resonator
   (a) computation of the outgoing and incoming velocities $u_{i>0}^{(n+1)+}$ and $u_{i<N_x}^{(n+1)-}$ using the numerical scheme (28);

Table III. Physical and geometrical parameters of the lip model.

m (kg)	k (N/m)	r (N.s/m)
$1.78 \cdot 10^{-4}$	1278.8	experiment dependent
l (m)	A (m²)	p_m (Pa)
10^{-2}	10^{-4}	experiment dependent
y_0 (m)	y_1 (m/s)	y_{eq} (m)
$4 \cdot 10^{-3}$	-4	$5 \cdot 10^{-4}$

    (b) computation of the incoming pressure at the input of the instrument $p_0^{(n+1)-}$ according to (2);

    (c) update of $u_{N_x}^{(n+1)-}$ at $x = D$, according to the reflection condition (14d).

2. Exciter
   (a) calculus of the lips aperture y_{n+1} in (50) based on the Newmark method and on the pressure at the entry of the resonator p_e^{n+1} (47);
   (b) calculus of the outgoing pressure at the resonator entry $p_0^{(n+1)+} = p_e^{n+1} - p_0^{(n+1)-}$ (43), where $p_0^{(n+1)-}$ is known according to step 1-(b) of the algorithm;
   (c) update of the forcing source $u_0^{(n+1)+}$ in the resonator (14c), based on $p_0^{(n+1)+}$ and (2).

3. Incrementation
   (a) computation of the time step Δt, according to the CFL condition (31);
   (b) update of the arrays.

4.2. Configuration

The wave propagation is described by the complete Menguy-Gilbert model in a resonator with a constant radius $R = 7$ mm. The parameters of the lip model are given in Table III. These parameters are issued from different publications [42, 43], and also from trial and error until self-oscillations are obtained.

The output of the model is the acoustic velocity at the end of the tube $u(D, t) = u^+(D, t) + u^-(D, t)$. Considering that the open end of the tube radiates as a monopole, $u(D, t)$ is converted into $p_{rec}(t)$, the pressure measured at an arbitrary distance $D_{rec} = 10$ m from the output of the tube, through the relation

$$p_{rec}(t) = \frac{\rho_0 \, S}{4\pi \, D_{rec}} \frac{\partial u}{\partial t}(D, t). \quad (55)$$

Equation (55) is the simplest way to transform the air flow at the output of the resonator $u(D, t)$ into a physical quantity similar to acoustic pressure. This choice has no influence on the incoming wave and on the mechanism of self-sustained oscillations. In particular, it does not modify the playing frequencies and the spectral contents.

4.3. Results

Three numerical experiments are carried out in order to check the influence of the nonlinear wave propagation on the behavior of the model. Simulations are carried out on

Scilab and last around one hour for each computed second, when a recent desktop computer is used (Intel Core i5-4690, 3.5 GHz, 16 Go, 2015). Obviously, it is faster to compute one second of sound when the tube is discretized on a smaller set of points (here $N_x = 400$). Time domain signals $p_{rec}(t)$ presented in the following figures are originally registered with a variable time step, they are then resampled at a frequency $f_s = 44.1$ kHz.

In a first experiment, the blowing pressure $p_m(t)$ decreases for 4 s, from $p_m = 8$ kPa downto $p_m = 0$ kPa whereas $r = 9.43 \cdot 10^{-2}$ N.s.m^{-1}. Two regimes are considered: linear wave propagation ($b = 0$), and nonlinear wave propagation. Results are displayed in Figure 12. The recorded pressure p_{rec} displays radically different time envelopes in the two cases (left column, middle and bottom). The most striking is that the peak value of the enveloppe is six times larger in the nonlinear case. This is due to the waveform which possesses sharp peaks in the nonlinear case. However, the attack transients duration (defined as the time at which the enveloppe peak value is reached) is very close to 0.24 s in both cases. The enveloppes in the release phases have different shapes: quasi-affine in the linear case, and exponential in the nonlinear case. However, the extinction threshold, i.e. the value of the blowing pressure p_m below which the oscillation disappears, is the same for both cases ($t = 2.9$ s). This has carefully been checked by close inspection of the Figure 12. In the linear case, the signal is more symmetric with respect to zero. Moreover, the regime is slightly quasi-periodic in the nonlinear case for high oscillating amplitudes ($t < 1$ s). A closer view of the signals (right column) reveals typical waveforms with sharp peaks in the nonlinear case.

Based on these data, two descriptors are computed in the frequency domain and displayed in Figure 13: the playing frequency (top) and the spectral centroid (bottom). During the attack phase, playing frequencies are superimposed. However, shortly after the enveloppe has reached its maximum value, a slight discrepancy is observed between the linear and nonlinear cases. The frequency difference observed is 3 cents, which is below the minimum audible difference, but this value increases all the larger as the starting value of the (decreasing) ramp of p_m is large. The influence of nonlinear propagation on the playing frequency vanishes progressively along with the decrease of the enveloppe amplitude.

The influence of the nonlinear propagation on the playing frequency has already been highlighted numerically in the case of the trombone [45] but only for steady state regimes, yet with a simplified model for the nonlinear propagation. Deviations of less than 5 cents for weak dynamics have been reported and are in agreement with our observations. We show here that the picture appears to be similar during the transient phase, as explained above. Note that a discussion of nonlinear propagation effects in the trombone using transients is given in [46].

The bottom picture in Figure 13 confirms that the nonlinear propagation is associated with an enrichment of the sound spectrum with high frequencies. Indeed the spec-
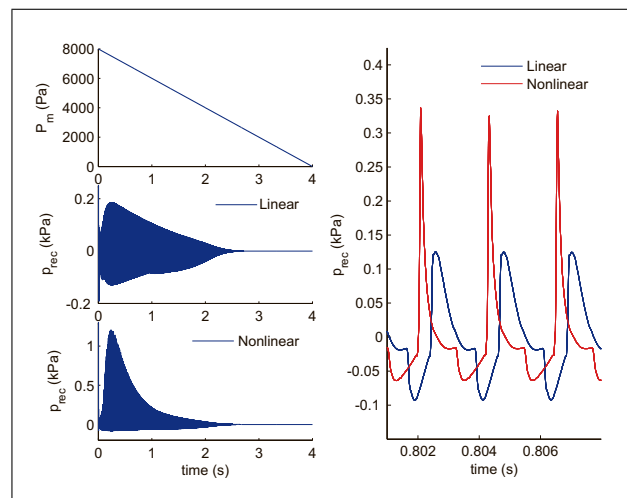

Figure 12. Progressive decrease in the blowing pressure, from $p_m = 8$ kPa downto $p_m = 0$ kPa. Left: time histories of p_m (top), p_{rec} with linear wave propagation (middle), and with nonlinear wave propagation (bottom). Right: zoom on a few periods of p_{rec} in the linear and nonlinear cases.
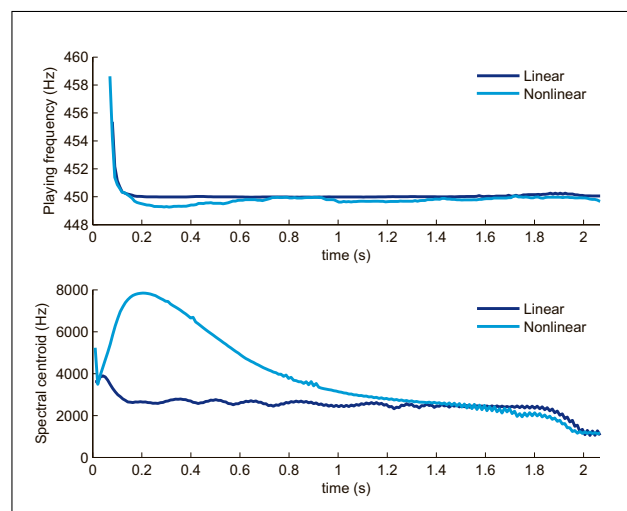

Figure 13. Descriptors calculated with the MIR Toolbox [44] based on the time domain signals presented in Figure 12. Top: playing frequency; bottom: spectral centroid.

tral centroid is up to three times higher than in the case of linear propagation. Moreover in the case of linear propagation, the spectral centroid is nearly constant, which confirms that the nonlinearity due to the exciter (47) cannot explain the spectral enrichment features of brassy sounds. This is not obvious since the brass model is always nonlinear (equation (47)), regardless of whether nonlinear propagation is considered. Therefore higher harmonics could be generated when the blowing pressure is increased. On the contrary, in the case of nonlinear propagation, the spectral centroid is a monotonic function of the oscillating amplitude. From $t = 1.4$ s, the amplitudes obtained using linear and nonlinear models are small; see Figure 12. Consequently, the nonlinear effects in the resonator become
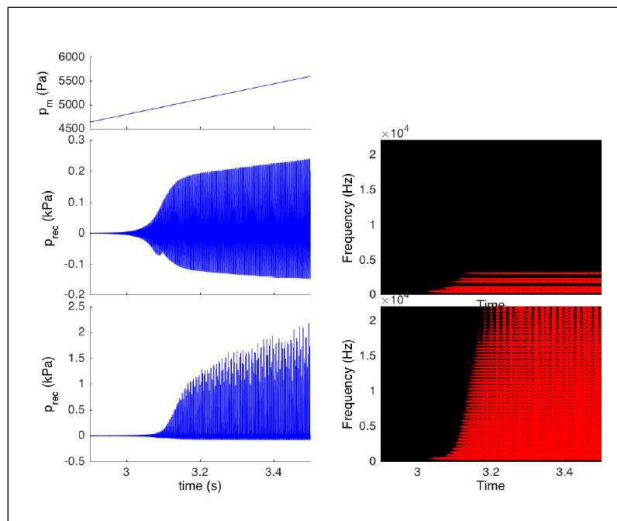
Figure 14. Progressive increase in the blowing pressure from $p_m = 0$ kPa to $p_m = 8$ kPa for 5 s (only a zoom is shown around the emergence of the oscillation). Left: time histories of p_m (top), p_{rec} with linear wave propagation (middle) and with nonlinear wave propagation (bottom). Right: spectrogram of p_{rec} in the case of linear (middle) and nonlinear wave propagation (bottom).
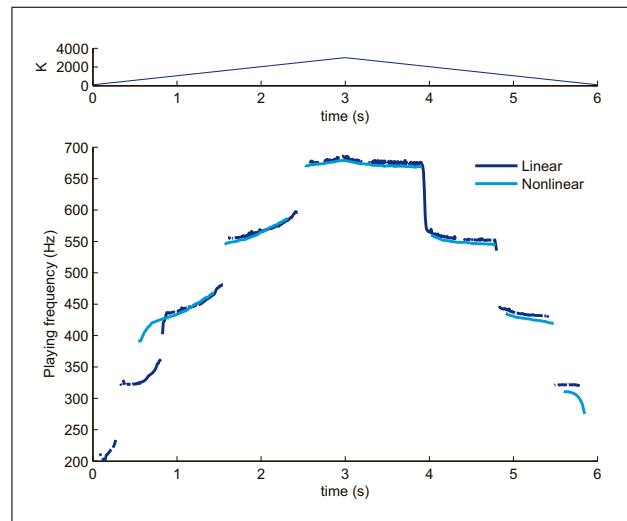

Figure 15. Symmetric increase / decrease in the stiffness of the lip model between $k = 100$ N.m^{-1} and $k = 3000$ N.m^{-1}. The blowing pressure is constant: $p_m = 20$ kPa. Top: time history of k. Bottom: time history of the playing frequency with linear wave propagation (dark blue) and in the case of nonlinear wave propagation (cyan). The damping coefficient is $r = 3.34 \cdot 10^{-2}$ N.s/m.

negligible. This explains why the centroids in both cases are almost the same.

A second numerical experiment is carried out by linearly increasing p_m from $p_m = 0$ kPa to $p_m = 8$ kPa for 5 s in the linear case ($b = 0$ in (14a)) and in the nonlinear case. The damping coefficient is $r = 6.67 \cdot 10^{-2}$ N.s/m. Close views around the emergence of the oscillation of time domain signals are presented in Figure 14 (left column). A remarkable feature is the fact that the oscillation occurs in linear and nonlinear cases for the same value of p_m. This result could appear obvious since the consequences of the nonlinear propagation are expected to vanish at the oscillation threshold where $b(u^{\pm})^2/2 \ll a|u^{\pm}|$ in (14a). However, it has been shown in [47, 48] that when the blowing pressure varies in time, counterintuitive results may be observed. Indeed, for a lower number of points on the spatial grid N_x, oscillation may not emerge anymore at the same value of the blowing pressure. For instance, apressure difference of 800 Pa is observed between linear and nonlinear cases when N_x is reduced to $N_x = 100$. In the right column of Figure 14, the spectrograms of the time signals highlight two major features: first, the signal calculated while considering nonlinear propagation has a much more broadband structure. Secondly, the spectral content evolves more significantly with the amplitude of the signal in the case of nonlinar propagation. This is consistent with experimental observations in brass instruments [3, 5].

In a third experiment, a constant blowing pressure $p_m = 20$ kPa is considered and the damping coefficient is $r = 3.34 \cdot 10^{-2}$ N.s.m^{-1}. The stiffness k of the lip model follows a symmetric increase / decrease for 6 s between $k = 100$ N.m^{-1} and $k = 3000$ N.m^{-1}, as shown in Figure 15 (top). As expected, the model plays on different

periodic regimes (corresponding to the 2nd to the 6th registers), the frequencies of which are displayed in the bottom picture. The most striking result is that for the parameter values chosen for the simulation, the lowest register is not playable in the case of nonlinear propagation (and the second register either when k is increased). A closer view reveals that for each register, frequency jumps with the neighbouring registers (lower and upper) do not occur at the same thresholds. Concerning the playing frequencies, differences may be weak but clearly audible, and differences are all the larger as the playing frequency (i.e. the register) is low: up to 13 cents on the 6th register, up to 23 cents on the 5th, up to 36 cents on the 4th, up to 114 cents on the 3rd. The playing frequency is always lower in the case of nonlinear propagation when k is decreased. When k is increased, for each register, the playing frequency is lower in the case of nonlinear propagation for the first half of the register. However, since it increases faster than in the case of linear propagation, the playing frequency in the case of nonlinear propagation becomes higher in the second half of the register. Here again, considering nonlinear propagation appears to have a noticeable effect during transients of a control parameter.

In order to highlight hysteresis effects, the same data is plotted with respect to the resonance frequency of the lip model in Figure 16 for linear (left) and nonlinear propagation (right). Hysteresis in such experiments is known to result from two mechanisms: the coexistence of stable periodic regimes and the variation with time of the bifurcation parameter (dynamic bifurcations). The left part of the figure shows familiar simulation results [49]. Considering the nonlinear propagation does not alter significantly the hysteresis.
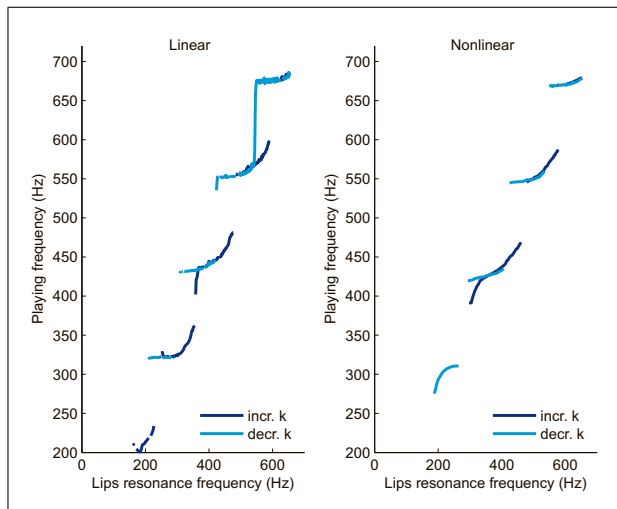
Figure 16. Same data than in Figure 15. Playing frequency is plotted with respect to the lip resonance frequency $(1/2\pi)\sqrt{k/m}$ with linear propagation ($b = 0$ in (14a)) (left) and in the case of nonlinear propagation (right).

5. Conclusion

A time-domain numerical modeling of brass instruments has been proposed. The propagation of outgoing and incoming nonlinear acoustic waves has been considered, taking into account the viscothermal losses at the boundaries of the resonator. The coupling with a model of lips has also been modeled, enabling simulations of the self-sustained oscillations in brass instruments. The software so obtained has been extensively tested. Preliminary applications to configurations of interest in musical acoustics have been demonstrated.

In its current form, our simulation tool can be used to investigate various open questions in acoustics. The first one concerns the frequency response of a nonlinear acoustical resonator, which has already been the subject of experimental and theoretical work [50, 35]. For this purpose, the methodology followed to determine the linear impedance (section 2.4.3) can be adapted to the nonlinear regime. A second application is the numerical study of the threshold of oscillations in brass instruments. Based on a modal representation of the field in the resonator, a Floquet theory can be applied in the linear regime [51]. However, to our knowledge, there are no known results when the nonlinearity of the wave propagation is taken into account. On the contrary, the numerical tool does not suffer from such a limitation.

Physical modeling also has to be improved. The radiation condition at the bell is elementary. More realistic models can be incorporated in our approach; see e.g. the section III-E in [25]. Moreover, considering simple outgoing and incoming waves in a tube with a variable section is a crude assumption. In the linear regime of propagation, the Webster-Lokshin wave equation provides a more realistic framework [52]. Extension of this equation to the nonlinear regime of propagation has been considered

by Bilbao and Chick, [25] but without the viscothermal losses. The derivation of the full bidirectional system—incorporating nonlinear wave propagation, and viscothermal losses in a variable tube—is the subject of current research.

References

[1] J. C. Risset, M. V. Mathews, Analysis of instrument tones, Physics Today **22**-2 (1969) 22–30.

[2] J. W. Beauchamp: Analysis of simultaneous mouthpiece and output waveforms. 66th Convention of the Audio Engineering Society (1980) 1–11.

[3] A. Hirschberg, J. Gilbert, R. Msallam, A. P. J Wijnands: Shock waves in trombones. J. Acoust. Soc. Am. **99**-3 (1996) 1754–1758.

[4] J. Gilbert, J. F. Petiot: Nonlinéarités dans les instruments de type cuivre; résultats expérimentaux. Actes de Colloque du Quatrième Congrès Français d'Acoustique, Marseille, 1997.

[5] P. L. Rendón, R. Ezeta, A. Pérez-López: Nonlinear sound propagation in trumpets. Acta Acust. united Ac. **99** (2013) 607–614.

[6] M. Campbell, J. Chick, J. Gilbert, J. Kemp, A. Myers, M. Newton: Spectral enrichment in brass instruments due to nonlinear sound propagation; a comparison of measurements and predictions. Proceedings of ISMA, Le Mans, 2014.

[7] L. Norman, J. Chick, D. Campbell, A. Myers, J. Gilbert: Player control of brassiness at intermediate dynamic levels in brass instruments. Acta Acust. united Ac. **96**-4 (2010) 614–621.

[8] C. Vergez, X. Rodet: New algorithm for nonlinear propagation of a sound wave; application to a physical model of a trumpet. Journal of Signal Processing **4**-1 (2000) 79–87.

[9] R. Msallam, S. Dequidt, R. Caussé, S. Tassart: Physical model of the trombone including nonlinear effects; application to the sound synthesis of loud tones. Acta Acust. united Ac. **86**-4 (2000) 725–736.

[10] T. Hélie, V. Smet: Simulation of the weakly nonlinear propagation in a straight pipe; application to a real-time brassy audio effect. MED Conference on Control and Automation, Ajaccio, 2008.

[11] S. Bilbao: Time-domain simulation of brass instruments. Proceedings of Forum Acusticum, Aalborg, 2011.

[12] A. Myers, R. Pyle, J. Gilbert, M. Campbell, J. Chick, S. Logie: Effects of nonlinear sound propagation on the characteristic timbres of brass instruments. J. Acoust. Soc. Am. **131**-1 (2012) 678–688.

[13] J. Gilbert, L. Menguy, M. Campbell: A simulation tool for brassiness studies. J. Acoust. Soc. Am. **123** (2008) 1854–1857.

[14] J. Chick, S. Logie, M. Campbell, J. Gilbert: Spectral enrichment and wall losses in trombones played at high dynamic levels. Proceedings of Acoustics 2012, 2012.

[15] M. W. Thompson, W. J. Strong: Inclusion of wave steepening in a frequency-domain model of trombone sound production. J. Acoust. Soc. Am. **110**-1 (2001) 556–562.

[16] L. Menguy, J. Gilbert: Weakly nonlinear gas oscillations in air-filled tubes; solutions and experiments. Acta Acust. united Ac. **86**-5 (2000) 798–810.

[17] L. Menguy: Propagation acoustique non linéaire dans les guides monodimensionnels. PhD Thesis, University of Maine, France, 2001.

[18] E. Godlewski, P. A. Raviart: Numerical Approximation of Hyperbolic Systems of Conservation Laws. Springer, 1996.

[19] D. Matignon: Représentations en variables d'état de modèles de guides d'ondes avec dérivation fractionnaire. PhD Thesis, University Paris 11, 1994.

[20] D. Matignon: An introduction to fractional calculus. Scaling, Fractals and Wavelets (Digital Signal and Image Processing Series), ISTE-Wiley, 2008.

[21] E. M. Abulwafa, M. A. Abdou, A. A. Mahmoud: Nonlinear fluid flows in pipe-like domain problem using variational-iteration method. Chaos, Solitons and Fractals **32** (2007) 1384–1397.

[22] N. Sugimoto: Burger's equation with a fractional derivative; hereditary effects on nonlinear acoustic waves. J. Fluid. Mech. **225** (1991) 631–653.

[23] B. Lombard, J. F. Mercier: Numerical modeling of nonlinear acoustic waves in a tube connected with Helmholtz resonators. J. Comput. Phys. **259** (2014) 421–443.

[24] O. Richoux, B. Lombard, J.F. Mercier: Generation of acoustic solitary waves in a lattice of Helmholtz resonators. Wave Motion **56** (2015) 85–99.

[25] S. Bilbao, J. Chick: Finite difference time domain simulation for the brass instrument bore. J. Acoust. Soc. Am. **134**-5 (2013) 386–3871.

[26] S. J. Elliott, J.M. Bowsher: Regeneration in brass wind instruments. J. Sound Vib. **83**-2 (1982) 181–217.

[27] A. Chaigne, J. Kergomard: Acoustics of Musical Instruments. Springer, 2016.

[28] M. F. Hamilton, D. T. Blackstock: Nonlinear Acoustics. Academic Press, 1998.

[29] W. Chester: Resonant oscillations in closed tubes. J. Fluid Mech. **18** (1964) 44–64.

[30] K. Diethelm: An investigation of some nonclassical methods for the numerical approximation of Caputo-type fractional derivatives. Numer. Algor. **47** (2008) 361–390.

[31] R. J. LeVeque: Numerical methods for conservation laws. Birkhäuser-Verlag, 1992.

[32] E. F. Toro: Riemann Solvers and Numerical Methods for Fluid Dynamics, A Practical Introduction. Springer, 1999.

[33] E. Sousa: The controversial stability analysis. Appl. Math. Comput. **145** (2003) 777–794.

[34] R. J. LeVeque: Finite Volume Methods for Hyperbolic Problems. Cambridge University Press, 2002.

[35] M. F. Hamilton, Y. A. Ilinskii, E. A. Zabolotskaya: Linear and nonlinear frequency shifts in acoustical resonators with varying cross sections. J. Acoust. Soc. Am. **110**-1 (2001) 109–119.

[36] G. B. Whitham: Linear and Nonlinear Waves. John Wiley & Sons, 1974.

[37] A. Hirschberg, J. Kergomard, G. Weinreich (Eds.): Mechanics of Musical Instruments (Chap. 7). Springer-Verlag, 1995.

[38] M. E. McIntyre, R. T. Schumacher, J. Woodhouse: On the oscillations of musical instruments. J. Acoust. Soc. Amer. **74** (1983) 1325–1345.

[39] C. Vergez: Trompette et trompettiste : un système dynamique non linéaire à analyser, modéliser et simuler dans un contexte musical. PhD Thesis, University Paris 6, France, 2000.

[40] V. Chatziioannou, M. van Walstijn: Energy conserving schemes for the simulation of musical instrument contact dynamics. J. Sound Vibration **339** (2015) 262–279.

[41] N. M. Newmark: A method of computation for structural dynamics. J. Eng. Mech. Div. ASCE **85**-3 (1959) 67–94.

[42] S. Adachi, M. Sato: Trumpet sound simulation using a two-dimensional lip vibration model. J. Acoust. Soc. Amer. **99** (1996) 1200–1209.

[43] C. Vilain, X.Pelorson, A.Hirschberg, L. Le Marrec, W. Op't Root, J. Willems: Contribution to the physical modeling of the lips; influence of the mechanical boundary conditions. Acta Acust. united Ac. **89** (2003) 882–887.

[44] O. Lartillot, MIR toolbox 1.5 User's Manual, 2013.

[45] R. Msallam, S. Dequidt, R. Caussé, S. Tassart: Physical model of the trombone including nonlinear effects; application to the sound synthesis of loud tones. Acta Acust. united Ac. **86**-4 (2000) 725–736.

[46] P. L. Rendón, F. Orduña-Bustamante, D. Narezo, A. Pérez-López, J. Sorrentini: Nonlinear progressive waves in a slide trombone resonator. J. Acoust. Soc. Am. **127**-2 (2010) 1096–1103.

[47] B. Bergeot, A. Almeida, C. Vergez, B. Gazengel: Prediction of the dynamic oscillation threshold in a clarinet model with a linearly increasing blowing pressure. Nonlinear Dynamics **73** (2013) 521–534.

[48] B. Bergeot, A. Almeida, C. Vergez, B. Gazengel: Prediction of the dynamic oscillation threshold in a clarinet model with a linearly increasing blowing pressure; influence of noise. Nonlinear Dynamics **74** (2013) 591–605.

[49] F. Silva, C. Vergez, P. Guillemain, J. Kergomard, V. Debut: MoReeSC: A Framework for the Simulation and Analysis of Sound Production in Reed and Brass Instruments. Acta Acust. united Ac. **100** (2014) 126–138.

[50] Y. A. Ilinskii, B. Lipkens, T. S. Lucas, T. W. Van Doren, E. A. Zabolotskaya: Nonlinear standing waves in an acoustical resonator. J. Acoust. Soc. Am. **104** (1998) 2664–2674.

[51] B. Ricaud, P. Guillemain, J. Kergomard, F. Silva, C. Vergez: Behavior of reed woodwind instruments around the oscillation threshold. Acta Acust. united Ac. **95**-4 (2009) 733–743.

[52] H. Haddar, D. Matignon: Efficient solution of a wave equation with fractional-order dissipative term. J. Comput. App. Math. **234** (2010) 2003–2010.